Exoskeletal Force Sensing End-Effectors with Embedded Optical Fiber Bragg Grating Sensors

Yong-Lae Park, *Student Member, IEEE,* Seok Chang Ryu, Richard J. Black, *Member, IEEE,*
Kelvin K. Chau, *Member, IEEE,* Behzad Moslehi, *Senior Member, IEEE,* and Mark R. Cutkosky, *Member, IEEE*

***Abstract*—Force sensing is an essential requirement for dexterous robot manipulation. We describe composite robot end-effectors that incorporate optical fibers for accurate force sensing and location of contact locations. The design is inspired by the sensors in arthropod exoskeletons that allow them to detect contacts and loads on their limbs. We present a fabrication process that allows us to create hollow multi-material structures with embedded fibers and we present the results of experiments for characterizing the sensors and controlling contact forces in a system involving an industrial robot and a two-fingered dexterous hand. We also described briefly the optical interrogation method used for measuring multiple sensors along a single fiber at kHz rates for closed-loop force control.**

***Index Terms*—Force and Tactile Sensing, Force Control, Dexterous Manipulation, Fiber Bragg Grating (FBG), Shape Deposition Manufacturing, Biologically-Inspired Robots.**

I. Introduction

FUTURE robots are expected to free human operators from difficult and dangerous tasks requiring dexterity in various environments. Prototypes of these robots already exist for applications such as extra-vehicular repair of manned spacecraft and robotic surgery, in which accurate manipulation is crucial. Ultimately, we envision robots operating tools with levels of sensitivity, precision and responsiveness to unexpected contacts that exceed the capabilities of humans, making use of numerous force and contact sensors on their arms and fingers.

However, compared to even the simplest of animals, today's robots are impoverished in terms of their sensing abilities. For example, a spider can contain as many as 325 mechanoreceptors on each leg [4], [18], in addition to hair sensors and chemical sensors [3], [52]. Mechanoreceptors such as the slit sensilla of spiders [4], [8] and campaniform sensilla of insects [37], [53] are especially concentrated near the joints, where they provide information about loads imposed on the limbs – whether due to regular activity or unexpected events such as collisions. By contrast, robots generally have a modest number of sensors, often associated with actuators or concentrated in devices such as a force sensing wrist. (For example, the Robonaut humanoid robot has 42 sensors in its hand and wrist module [9].) As a result, robots often respond poorly to unexpected and arbitrarily-located impacts. The work in this paper is part of a broader effort aimed at creating light-weight, rugged appendages for robots that, like the exoskeleton of an insect, feature embedded sensors so that the robot can be more aware of both anticipated and unanticipated loads in real time.

Part of the reason for the sparseness of force and touch sensing in robotics is that traditional metal and semiconductor strain gages are tedious to install and wire. The wires are often a source of failure at joints and are receivers for electromagnetic noise. The limitations are particularly severe for force and tactile sensors on the fingers of a hand. Various groups have explored optical fibers for tactile sensing, where the robustness of the optical fibers, the immunity to electromagnetic noise and the ability to process information with a CCD or CMOS camera are advantageous [12], [26], [34]. Optical fibers have also been used for measuring bending in the fingers of a glove [24] or other flexible structures [11], where the light loss is a function of the curvature. In addition, a single fiber can provide a high-bandwidth pathway for taking tactile and force information down the robot arm [2].

We focus on a particular class of optical sensors, fiber Bragg grating (FBG) sensors, which are finding increasing applications in structural health monitoring [1], [29], [30] and other specialized applications in biomechanics [10], [13] and robotics [42], [44]. FBG sensors have been attached to or embedded in metal parts [17], [31] and in composites [55] to monitor forces, strains, and temperature changes. FBG sensors are particularly attractive for applications where immunity to electromagnetic noise, small size and resistance to harsh environments are important. Examples include space or underwater robots [16], [19], [56], medical devices (especially for use in MRI fields) [43], [63], and force sensing on industrial robots with large motors operating under pulse-width modulated control [17], [64].

FBG sensors reflect light with a peak wavelength that shifts in proportion to the strain they are subjected to. The sensitivity of regular FBGs to axial strain is approximately 1.2 pm/$\mu\varepsilon$ at 1550 nm center wavelength [7], [28]. With the appropriate FBG interrogator, very small strains, on the order of $0.1\mu\varepsilon$, can be measured. In comparison to conventional strain gages, this sensitivity allows FBG sensors to be used in sturdy structures that experience modest stresses and strains under normal loading conditions. The strain response of FBGs is linear with no indication of hysteresis at temperatures up to 370°C [38] and, with appropriate processing, as high as 650°C [41]. Multiple FBG sensors can be placed along a single fiber

Y-L. Park, S. C. Ryu, and M. R. Cutkosky are with the Center for Design Research, Stanford University, Stanford, CA 94305, USA, e-mail: {ylpark, scryu, cutkosky}@stanford.edu.

R. J. Black, and B. Moslehi are with Intelligent Fiber Optic Systems Corp. (IFOS), Santa Clara, CA 95054, USA, e-mail: {rjb, bm}@ifos.com.

K. K. Chau was with IFOS and is now with Glimmerglass, Hayward, CA, 94545, USA, e-mail: chau@glimmerglass.com.

This paper is adapted, in part, from IEEE ICRA papers in 2007 and 2008.

and optically multiplexed at kHz rates.

To our knowledge, the work in this paper is the first application of FBG sensors in hollow, bio-inspired multi-material robot limbs. The rest of the article is organized as follows. Section II discusses design concepts for the force sensing finger prototype. Section III describes the fabrication process using a new variation of a rapid prototyping process. Section IV addresses the static and the dynamic characterization of the sensorized finger structures, including the ability to localize contact forces. Sections V and VI describe the hand controller used with the finger and the results of force control experiments. In Section VII, we present the results of our ongoing work to miniaturize the technology so that multiple FBG sensors can be applied to human-scale robotic fingertips or tools. In Section VIII, we discuss the optical interrogation technology for reading the strains from multiple sensors at sufficient rates for closed-loop force control. We conclude with a discussion of future work, which includes a potential extension of the finger prototype with a larger number of sensors for measurement of external forces and contact locations. Future work also includes extending the capability of the optical interrogator and using multi-core polymer fibers.

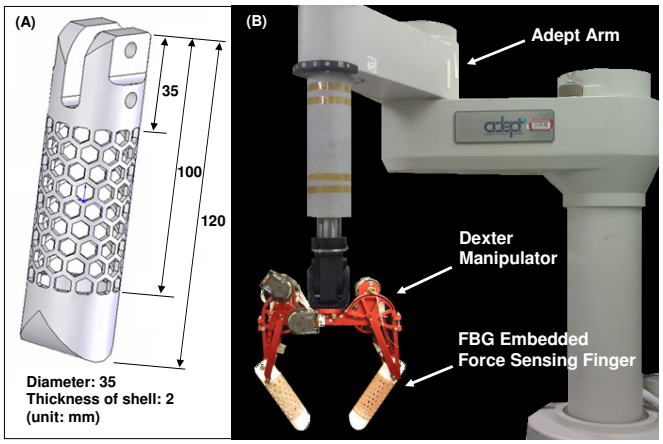

Fig. 1. (A) Prototype dimensions. (B) FBG embedded force sensing finger prototypes integrated with two fingered hand and industrial robot.

II. Design Concepts

Prototype fingers were designed as replacements for aluminum fingers on a two-fingered dexterous hand used with an industrial robot for experiments on force control and tactile sensing [20], as shown in Figure 1. Figure 2 shows a completed finger prototype including cross-sectional views. Each of the two fingers can be divided into three parts: fingertip, shell, and joint. The fingertip and shell are exoskeletal structures. Four FBG sensors are embedded in the shell for strain measurement, and one FBG sensor is placed at the center of the finger for temperature compensation. The remainder of this section describes the design features of the prototype including the exoskeleton structure, solutions for reducing creep and the effects of temperature variations, and sensor placement.

A. Exoskeleton Structure

In comparison to solid structures, exoskeletal structures have high specific stiffness and strength. In addition, unlike a solid beam, they exhibit distinct local, as well as global, responses to contact forces (Figure 3). This property facilitates the estimation of contact locations. The exoskeletal structure may be compared with the plastic fingertip described by Voyles et al. [57], which used electro-rheological fluids and capacitive elements for extrinsic tactile sensing and required an additional cantilever beam with strain gages for force-torque information.

To enhance the deformation in response to local contact forces, our exoskeleton is designed as a grid. Although a grid structure with embedded FBG sensors has been explored for structural health monitoring on a large scale [1], it has rarely been considered in robotics. The ribs of the grid are thick enough to encapsulate the optical fibers and undergo axial and bending strains as the grid deforms. Although various polygonal patterns including triangles and squares are possible, hexagons have the advantage of minimizing the ratio of perimeter to area [45], [21] and thereby reducing the weight of the part. Also, the hexagonal pattern avoids sharp interior corners, which could reduce the fatigue life. The thickness of the shell and the width of the pattern were determined so that each finger can withstand normal loads of at least 12 N.

B. Creep Prevention and Thermal Shielding

Polymer structures experience greater creep than metal structures. Creep adversely affects the linearity and repeatability of the sensor output. In addition, thermal changes will affect the FBG signals. Drawing inspiration from a polymer hand by Dollar et al. [15], a copper mesh (080X080C0055W36T, TWP Inc., Berkeley, CA, USA) was embedded into the shell, to reduce creep and provide some thermal shielding for the optical fibers. The high thermal conductivity of copper expedites the distribution of heat applied from outside the shell and creates a more uniform temperature within.

C. Strain Sensor Configuration

In general, larger numbers of sensors will provide more information and make the system more accurate and reliable. However, since additional sensors increase the cost and require more time and/or processing capacity, the optimal sensor configuration should be considered, as discussed by Bicchi [5]. In the present case, if we assume that we have a single point of contact, there are five unknown values: the longitude and latitude of a contact on the finger surface, and the three orthogonal components of the contact force vector in the X, Y, and Z directions. For the initial finger prototypes, we further simplify the problem by assuming the contact force is normal to the finger surface (i.e., with negligible friction). This assumption reduces the number of unknowns to three so that a minimum of three independent sensors are needed. In the prototype, four strain sensors were embedded in the shell.

Before fabrication, finite element analysis was conducted to determine the sensor locations. Figure 3 shows strain distributions when different types of forces are applied to the shell and to the fingertip. Strain is concentrated at the top of the shell where it is connected to the joint. The four sensors

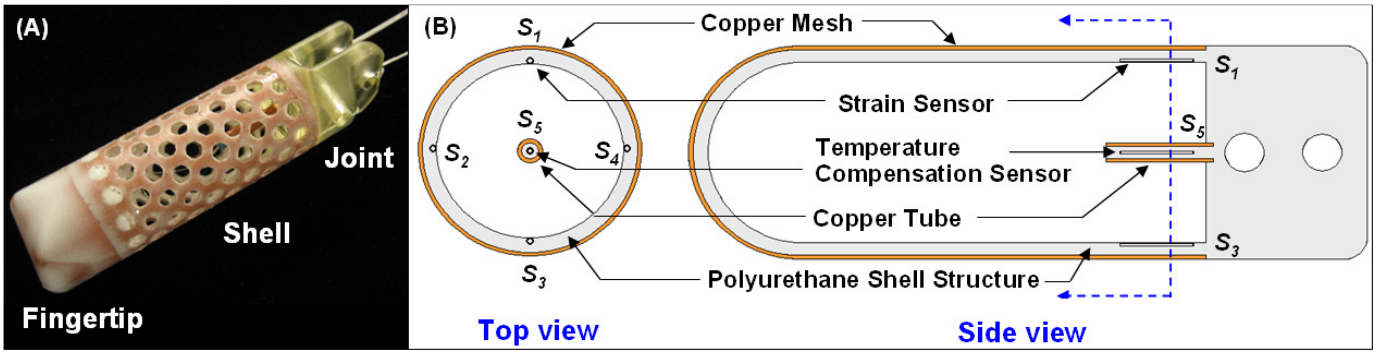

Fig. 2. (A) Finger prototype. (B) Cross-sectional views ($S_1 - S_4$: strain sensors, S_5: temperature compensation sensor). See Table I for sensor parameters.

were embedded at 90° intervals into the first rib of the shell, closest to the joint, as shown in Figure 2.

D. Temperature Compensation

Since embedded FBG sensors are sensitive to temperature, it is necessary to isolate thermal effects from mechanical strains. The sensitivity of regular FBGs to temperature change is approximately 10 pm/°C at 1550 nm center wavelength [22], [25]. Various complicated temperature compensation methods have been proposed, such as the use of dual-wavelength superimposed FBG sensors [60], saturated chirped FBG sensors [61], and an FBG sensor rosette [35]. We chose a simpler method that involved using an isolated, strain-free FBG sensor to measure thermal effects. Subtracting the wavelength shift of this sensor from that of any other sensor corrects for the thermal effects on the latter [47]. An important assumption in this method is that all the sensors experience the same temperature. Our prototype has one temperature compensation sensor in the hollow area inside the shell, as shown in Figure 2. Although it is distanced from the strain sensors, the previously mentioned copper heat shield results in an approximately uniform temperature within the shell. Since the temperature compensation sensor is encapsulated in a copper tube attached at one end to the joint, it experiences no mechanical strain.

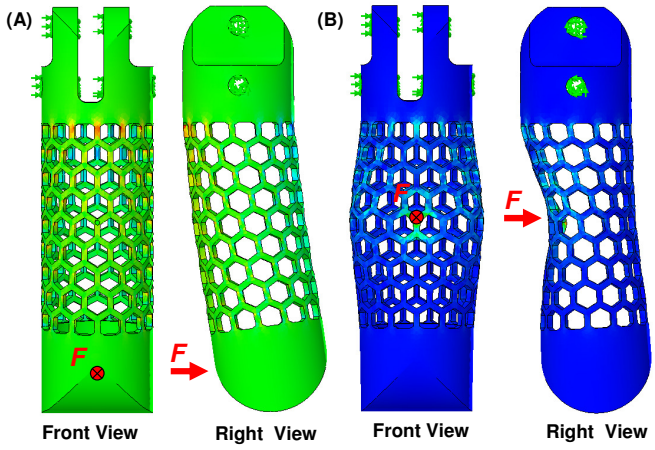

Fig. 3. Finite element models showing strain concentrations on the first rib closest to the fixed joint. (A) Point load is applied to the fingertip. (B) Point load is applied to the middle of the shell structure.

III. SDM Fabrication Procedure

The finger prototype was fabricated using a variation of the SDM rapid-prototyping process [58] to make a hollow three-dimensional part. The prototype was cast in a three step process, shown in Figure 4, with no direct machining required.

The base material is polyurethane, chosen for its combination of fracture toughness, ease of casting at room temperature and minimal shrinkage. In particular, the urethane has a low mixed viscosity (150 cps), which helps it to completely fill the narrow channels associated with ribs in the grid structure.

The first step is to cast the shell (1.a-1.d in Figure 4). The outer mold is made of hard wax to maintain the overall shape. The inner mold is hollow and made of silicone rubber, which can be manually deformed and removed when the polyurethane is cured. The optical fibers and copper mesh were embedded in this step. Although it is often preferable to strip the 50μm polyimide coating on FBG regions before optical fibers are embedded, we found that adequate bonding was obtained between the polyurethane and the coated fibers, and the amount of creep was negligible compared to overall deformation and creep in the urethane structure. Retaining the coating also protected the fibers during the casting process.

The second step is fingertip casting (2.a-2.d), which uses separate molds and occurs after the shell is cured. The polyurethane for the fingertip bonds to the cured shell part.

In the final step, the joint is created (3.a-3.c). As with the fingertip, the joint bonds to the cured shell. Since the joint is not hollow, an inner mold is not needed. Because the joint has no copper mesh, it is cast using hard polyurethane (Task 9, Smooth-On, Easton, PA, USA) to reduce creep. In comparison, the shell and fingertip were cast using a somewhat softer polyurethane (Task 3, Smooth-On) to enhance impact resistance. Figure 5 shows the molds and embedded copper mesh prepared for the modified SDM process. After each step, the polyurethane is cured at room temperature for 2 to 3 days.

TABLE I
Parameters of Embedded FBG Sensors

Sensor	Wavelength	Bandwidth	Reflectivity
S_1	1543.490 nm	0.380 nm	99.55 %
S_2	1545.207 nm	0.360 nm	99.34 %
S_3	1547.859 nm	0.370 nm	98.25 %
S_4	1549.925 nm	0.310 nm	97.70 %
S_5	1553.100 nm	0.400 nm	99.58 %

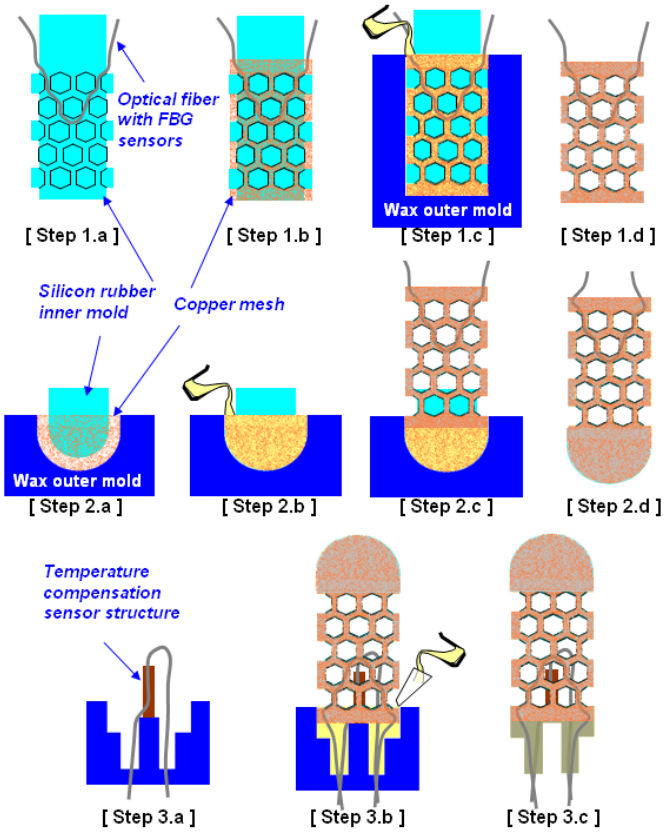

Fig. 4. Modified SDM fabrication process: [Step 1] Shell fabrication (a) Prepare silicone rubber inner mold and place optical fibers with FBG sensors (b) Wrap the inner mold with copper mesh (c) Enclose inner mold and copper mesh with a wax outer mold and pour liquid polyurethane (d) Remove inner and outer molds when polyurethane cures. [Step 2] Fingertip fabrication (a) Prepare inner and outer molds and place copper mesh (b) Cast liquid polyurethane (c) Place cured shell into the uncured polyurethane (d) Remove molds when the polyurethane cures. [Step 3] Joint fabrication (a) Prepare outer mold and place temperature compensation sensor structure (b) Place cured shell and fingertip into the uncured polyurethane (c) Remove outer mold when polyurethane cures.

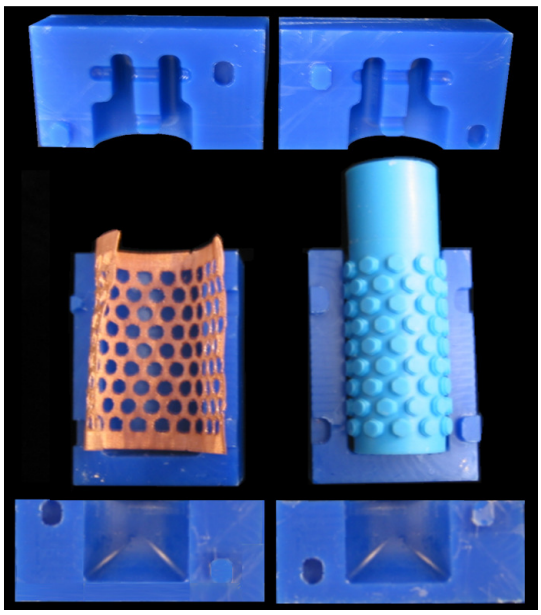

Fig. 5. Wax and silicone rubber molds and copper mesh used in modified SDM fabrication process.

IV. Static and Dynamic Characterization

The finger prototype was characterized with respect to static forces, modes of vibration, hysteresis, and thermal effects.

A. Static Force Sensing

Static forces were applied to two different locations on the shell and fingertip. Figure 6 shows the force locations and the responses of two sensors A and B, in the shell. Applying forces to the shell yielded sensitivities of 24 pm/N and -4.4 pm/N for sensors A and B, respectively. Sensor A, being on the same side of the shell as the contact force, had a much higher strain. Applying a force to the fingertip yielded sensitivities of 32 pm/N and -29 pm/N for sensors A and B, respectively. In this case, the location of the force resulted in roughly equal strains at both sensors. For a given location, the ratio of the sensor outputs is independent of the magnitude of the applied force. The effect of location is discussed further in Section IV-E. The optical interrogator can resolve wavelength changes of 0.5 pm or less, corresponding to 0.02 N at the shell and 0.016 N at the fingertip. However, considering the deviations from linear responses (RMS variations of 5.0 pm and 9.5 pm for the shell and the fingertip tests, respectively) the practical resolutions of force measurement are 0.10 N at the shell and 0.15 N at the fingertip. The difference between the minimum detectable force changes and the practical resolution for force sensing are due to a combination of effects including creep in the polymer structure, hysteresis and thermal drift over the 30 minute test cycle. These effects are discussed further in the following sections.

B. Modes of Vibration

Prior to setting up a closed-loop control system, we investigated the dynamic response of the fingers. Figure 7 shows the

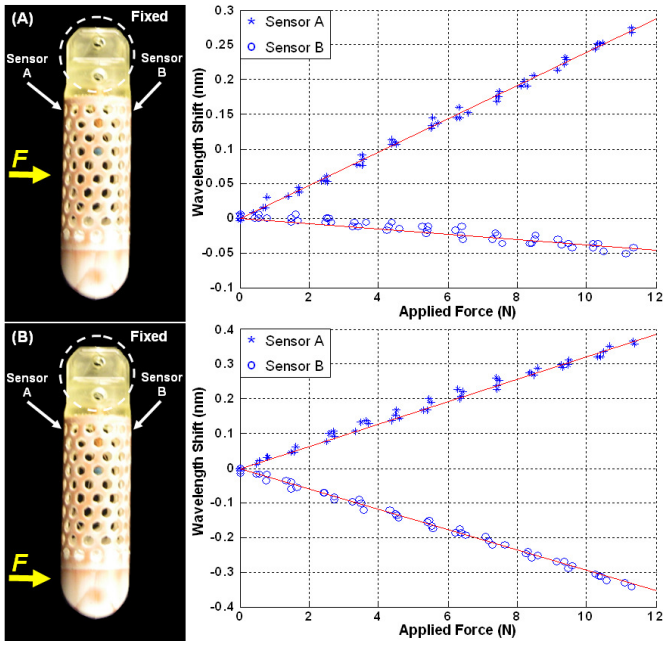

Fig. 6. Static force response results. (A) Shell force response. (B) fingertip force response.

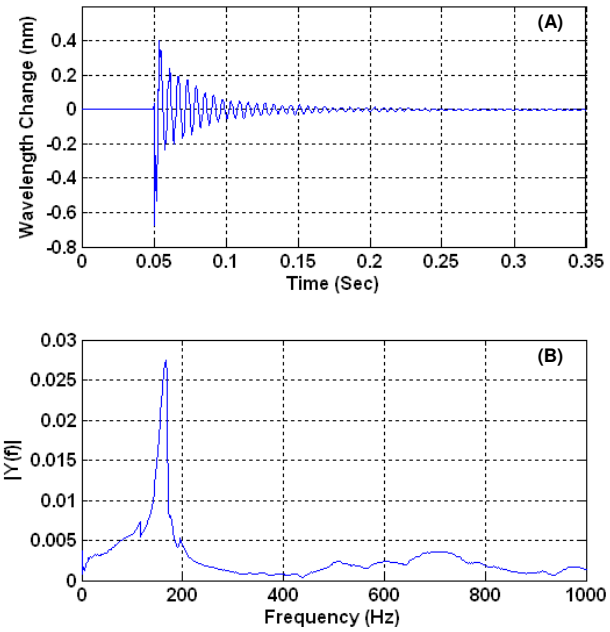

Fig. 7. (A) Impulse response of the finger prototype. (B) Fast Fourier transform of impulse response.

impulse response (expressed as a change in the wavelength of light reflected by an FBG cell) and its fast Fourier transform (FFT). The impulse was effected by tapping on the finger with a light and stiff object, a pencil. The FFT shows a dominant frequency around 167 Hz, which is a result of the dominant vibration mode.

A finite element analysis (Figure 8) indicates that there are two dominant vibration modes corresponding to the orthogonal X and Y bending axes, with nearly equal predicted frequencies of just over 180 Hz. The difference between the computed and measured frequency is due to the imperfect modeling of the local stiffness of the polymer/mesh composite. The actual stiffness of the composite depends on manufacturing tolerances including the location of the mesh fibers within the polymer structure.

C. Hysteresis Analysis

Polymer structures in general are subject to a certain amount of creep and hysteresis, which is one reason why they have traditionally been avoided for force sensing and control applications. In the present case, these effects are mitigated by

	1	2	3	4	5
Mode	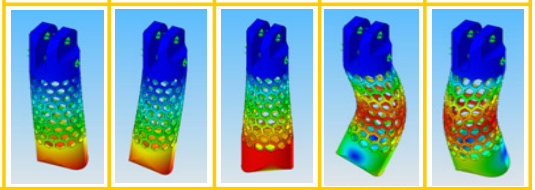				
Frequency	**181.2** Hz	**185.1** Hz	479.1 Hz	938.7 Hz	941.5 Hz

Fig. 8. Modes of vibration of the finger prototype using finite element analysis. Modes 1 and 2 are the dominant modes, representing bending about X and Y axes, respectively.

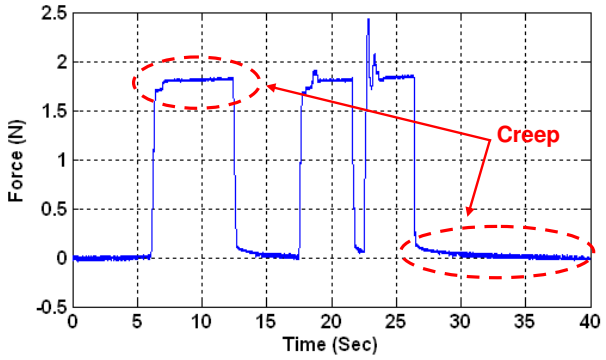

Fig. 9. The effect of applying a steady load for several seconds and suddenly removing it from the polymer fingertip.

embedding a copper mesh within the structure. However, there is still some creep and hysteresis as shown in Figures 9 and 10. The plot in Figure 9 was produced by applying a moderate load of approximately 1.8 N to the finger for several seconds and then removing it suddenly. Figure 10 shows detailed views of loading and unloading periods. The measured force was obtained by optically interrogating the calibrated FBG sensors.

When a steady load is applied for several seconds there is a small amount of creep, part of which also arises from imperfect thermal compensation. The effect is relatively small over periods of a few seconds, corresponding to typical grasping durations in a pick-and-place or manipulation task. A more significant effect occurs when the load is released. As the plot indicates in Figure 10 (B), the force quickly drops to a value of approximately 0.1 N and then more slowly approaches zero. To overcome this effect in manipulation tasks, a simple strategy was employed. Whenever the force suddenly dropped to a small value (less than 0.17 N), we assumed that contact had been broken. At this point, we reset the zero-offset after a brief time delay. As described in the following section, loss of contact is also a signal to switch the robot from force control to position control.

D. Temperature Compensation

Figure 11 shows a typical thermal test result. Over a three minute period, the fingertip was loaded and unloaded

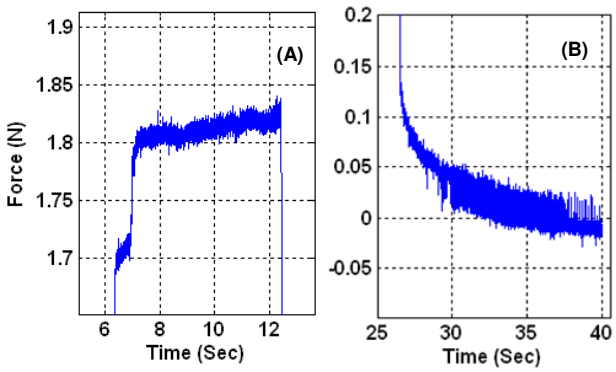

Fig. 10. Detailed views of creep under steady loading (A) and of the hysteresis associated with sudden unloading (B).

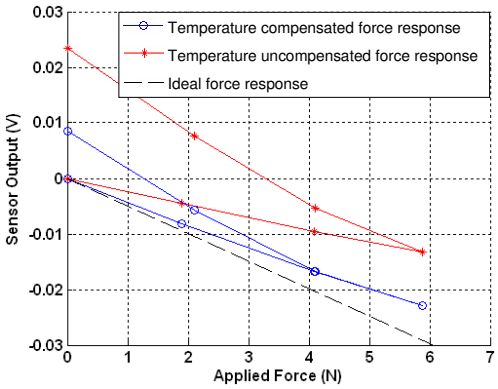

Fig. 11. Test result showing partial temperature compensation provided by the central sensor.

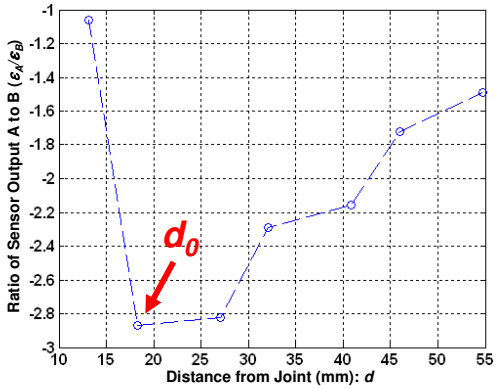

Fig. 13. Strain ratio of sensor A to B ($\varepsilon_A/\varepsilon_B$) for several locations of force application along length of the finger.

while the temperature was decreased from 28.3°C to 25.7°C. The ideal (temperature invariant) sensor output is indicated by the dashed line. The results show that the temperature compensation sensor reduces thermal effects. However, a more accurate compensation design is desired in the next prototype.

E. Contact Force Localization

It is useful to know the locations of contact forces when a robot is manipulating an object. It is also useful to distinguish, for example, between a desired contact on the fingertip and an unexpected contact elsewhere on the finger. Since the finger prototype has a cylindrical external shape, the location of a contact force can be expressed in terms of latitude and longitude. The following discussion assumes a single contact.

1) Longitudinal Location: Longitudinal localization requires some understanding of the structural deformation of the shell. Figure 12 shows simplified two-dimensional diagrams of the prototype. When a force is exerted at a certain location, as shown in (A), the structure will deform and sensors A and B will measure strains ε_A and ε_B, respectively as indicated. This situation can be decomposed into two separate effects, as shown in (B) and (C). By superposition, $\varepsilon_A = \varepsilon_1 + \varepsilon_2$ and $\varepsilon_B = \varepsilon_3$. Therefore, if the ratio of ε_A to ε_B is known, we can estimate d, the longitudinal force location. Figure 13 shows the plot of experimental ratios of ε_A to ε_B as a function of d.

There is some ambiguity in the localization, since two values of d result in the same ratio. However, if we let d_0 be the distance at which $\varepsilon_A/\varepsilon_B$ is minimized, and we restrict ourselves the region $d > d_0$, we can resolve this ambiguity. Further, if we modify the manufacturing process to place the sensors closer to the other surface of the shell, d_0 approaches 0 and we can localize an applied force closer to the joint.

2) Latitudinal Location: Latitudinal location can be approximated using centroid and peak detection as discussed by Son et al. [54]. Figure 14 (A) shows a cross-sectional view of the finger with four strain sensors and an applied contact force indicated. Figure 14 (B) shows its corresponding sensor signal outputs. The two sensors closest to the force location will experience positive strains (positive sensor output), and the other two sensors will experience negative strains (negative sensor output), regardless of the longitudinal location of the force, if $d > d_0$. However, since all the sensor signals must be non-negative to use the centroid method, all signal values must have the minimum signal value subtracted from them. With this, we can find the angular orientation theta of the contact force:

$$\theta = \frac{\sum \phi_i S_i'}{\sum S_i'} - \alpha$$

for $i = 1, 2, 3, 4$, where $S_i' = S_i - \min\{S_1, S_2, S_3, S_4\}$, $\phi_1 = \alpha$ and $\phi_k = \phi_{k-1} + \frac{\pi}{2}$, for $k = 2, 3, 4$ (if $\phi_k \geq 2\pi$, $\phi_k = \phi_k - 2\pi$), S_i is the output signal from sensor i, and α is the clockwise angle between sensor 1 and the sensor with the minimum output signal value.

This centroid and peak detection method produced errors of less than 2°, corresponding to less than 0.5 mm on the perimeter in both FEM simulation and experiments. However, the experimental data yielded an offset of approximately 5°

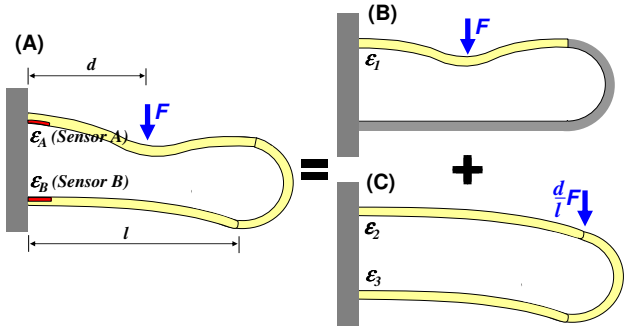

Fig. 12. 2D simplified shell structure and deformations of finger prototype.

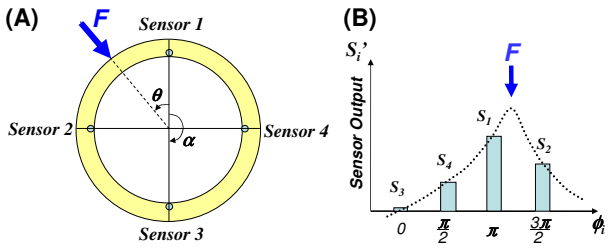

Fig. 14. (A) Top view of the prototype showing embedded sensors and force application. (B) Plot of sensor signal outputs.

while the simulation data yielded an offset of approximately 1.5°. The difference is likely due to manufacturing tolerances in the placement of the sensors.

V. Force Controller

Figure 15 shows the architecture of the hardware system. The two-fingered robot hand, Dexter, is a low-friction, low-inertia device designed for accurate force control. The hand is controlled by a process running under a real-time operating system (QNX) at 1000 Hz, which reads the joint encoders, computes kinematic and dynamic terms and produces voltages for linear current amplifiers that drive the motors [20].

The hand controller also acquires force information, via shared memory, from a process that obtains analog force information at 5 kHz from the optical interrogator (I*Sense, IFOS Inc., Santa Clara, CA, USA) that monitors FBG sensors.

The FBG interrogator is based on high-speed parallel processing using Wavelength Division Multiplexing (WDM). Multiple FBG sensors are addressed by spectral slicing, with the available source spectrum divided up so that each sensor is addressed by a different part of the spectrum. The interrogator built for this work uses sixteen channels of a parallel optical processing chip. Each channel is separated by 100 GHz (approximately 0.8 nm wavelength spacing around an operating wavelength of 1550 nm)[1] so that the total required source bandwidth is 12.8 nm. We provide further description of operating principles in Section VIII and describe how this approach can be adapted to support larger numbers of FBG sensors in a single fiber in the Appendix.

Dexter is mounted to a commercial AdeptOne-MV 5-axis industrial robot. Communication with the Adept robot is performed using the ALTER software package, which allows new positions to be sent to the Adept robot over an Ethernet connection every 16 ms (62.5 Hz). Due to this limitation, all force control is done within Dexter, and the Adept robot is used only for large motions and to keep Dexter approximately centered in the middle of the workspace.

[1]Operation is in the 1550-nm wavelength window (and, more specifically, within the C-band) to exploit the availability and low cost of components for telecom applications.

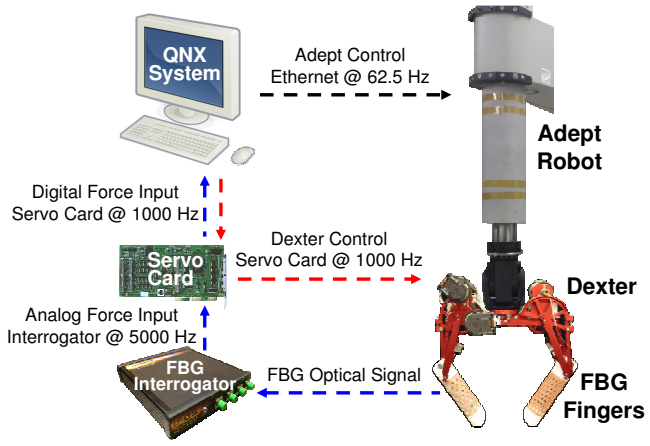

Fig. 15. Hardware system architecture.

When the fingers are not in contact with an object, the fingers are operated under computed-torque position control, with real-time compensation for gravity torques and inertial terms. When in contact, the fingers are switched over to a nonlinear force control as described in the next section.

VI. Contact Force Control

Most implementations of contact force control can be divided into two categories: impedance control and direct force control [62]. The impedance control [23], [27] aims at controlling position and force by establishing desired contact dynamics. Force control [46] commands the system to track a force setpoint directly. For this work, we adopted a nonlinear controller presented by our collaborator at NASA, the late H. Seraji [49], [50], [51]. When the system detects contact with the fingertip, it switches to force control as depicted in Figure 16. The system actually performs hybrid force/position control [32], [46] at this stage, as the position and force controllers are combined to control forces. The proportional-integral (PI) force controller is constructed as

$$K(s) = k_p + \frac{k_i}{s}$$

based on the first-order admittance

$$Y(s) = k_p s + k_i$$

where k_p and k_i are the proportional and integral force feedback gains, respectively. To make the force controller simple, we fix the proportional gain, k_p, to a constant and make the integral gain, k_i, a nonlinear function of the force error. The nonlinear integral gain is determined by the sigmoidal function

$$k_i = k_0 + \frac{k_1}{1 + \exp[-\mathrm{sgn}(\Delta) k_2 e]}$$

where e is the force error ($F_r - F$), $\Delta = F_r - F_s$, F_s is the steady value of the contact force before applying new F_r and k_0, k_1, and k_2 are user-specified positive constants that determine the minimum value, the range of variation, and the rate of variation of k_i, respectively. The value of $\mathrm{sgn}(\Delta)$ is +1 when $F_r > F_s$, and -1 when $F_r < F_s$.

We can achieve fast responses and small oscillations in control with this nonlinear gain since the nonlinearity provides high gains with large errors and low gains with small errors. To minimize oscillations due to large proportional gains when the switch occurs between position and force control, all gains except the integral force feedback gain are ramped from zero to the defined values over a transition time of 0.1 seconds.

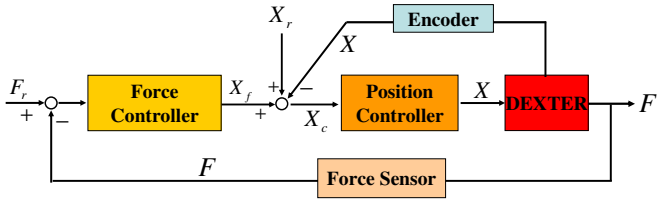

Fig. 16. Position based force control system. F and F_r are contact force and user-specified force setpoint. X, X_c, X_f , and X_r are respectively actual position, commanded position, position perturbation computed by the force controller, and reference position of the end-effector.

A. Results of Experiments

In this section, we present the results of two experiments that assess the accuracy of control achieved with the finger prototype. The first experiment shows how accurately the manipulator maintains a desired force during contact by comparing the force data from the prototype with that from a commercial 6-axis force-torque sensor (ATI-Nano25 from ATI Industrial Automation). The second experiment shows force control during manipulation tasks, including linear and rotational motions of the hand, while grasping an object.

1) Experiment 1 (Force Setpoint Tracking): The Adept arm moves in one direction until the fingertip touches the commercial load cell. As soon as the finger detects contact, the Adept arm stops and the Dexter hand switches to force control. After a period of time, the Adept arm moves away from the object and the hand switches back to position control. Figure 17 shows the horizontal motion of the Adept arm in parallel with the joint rotation of the distal joint of the Dexter hand and the force data from both the finger and the load cell. The result shows the force data from the finger and the load cell almost match exactly over the duration of the experiment. In addition, there is a small amount of slippage reflected in the mirror-image dynamic force signals reported by the finger and load cell, respectively, as the finger breaks the contact.

We note that to complete the experiment it was necessary to carefully shield and ground all wires emanating from the commercial load cell due to the large magnetic fields produced by the industrial robot.

2) Experiment 2 (Force Control during Manipulation): This experiment concerns the ability of the hand to maintain a desired grasp force while subject to motions in a manipulation task. The robot was commanded to lift the grasped object, a metal block weighing 100 g, move it horizontally a distance of approximately 30 cm, rotate it about the Z and Y axes, return the block to the original location, and replace it. In every case, the controller returned to the desired force within 0.01 seconds. The results of this experiment can be seen in Figure 18. The magnitude of the combined (X, Y, and Z) acceleration of the manipulator is plotted in parallel with the measured grasp force. Disturbances associated with the accelerations and decelerations along the path can be observed in the force data. The root-mean-square of force errors during the force control is < 0.03 N.

Since the current finger prototype is capable of control one-axis forces, more complicated force control experiments, in two or three axes, will be carried out in the future.

VII. Miniaturized Force Sensing Finger

Following the successful creation of large-scale (120 mm long) robot fingers, the next step was to produce human-scale fingertips for robots designed for human interaction in space. The same technology, having no metal components or electronics, could also be applied to robots for MRI procedures.

Figure 19 shows a prototype of a small fingertip with an embedded optical fiber containing FBG strain sensors. For this application, an 80 μm diameter bend-insensitive optical fiber from OFS was selected. These fibers tolerate comparatively

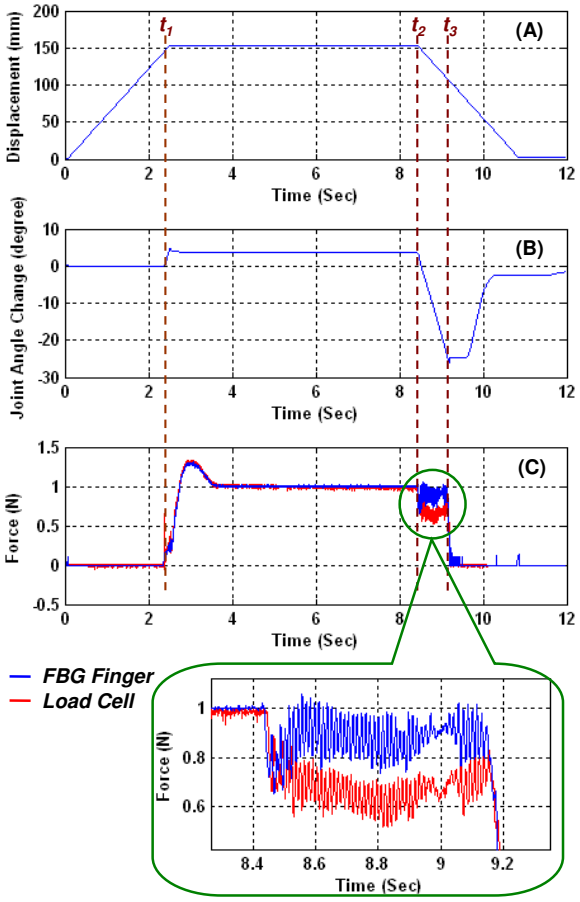

Fig. 17. Experimental results of force setpoint tracking. (A) Adept robot motion. (B) Joint angle change of Dexter manipulator. (C) Force data from load cell and FBG embedded robot finger prototype. Robot starts force control as soon as it makes a contact with the object at t_1. Robot starts to retreat at t_2. Robot breaks contact at t_3.

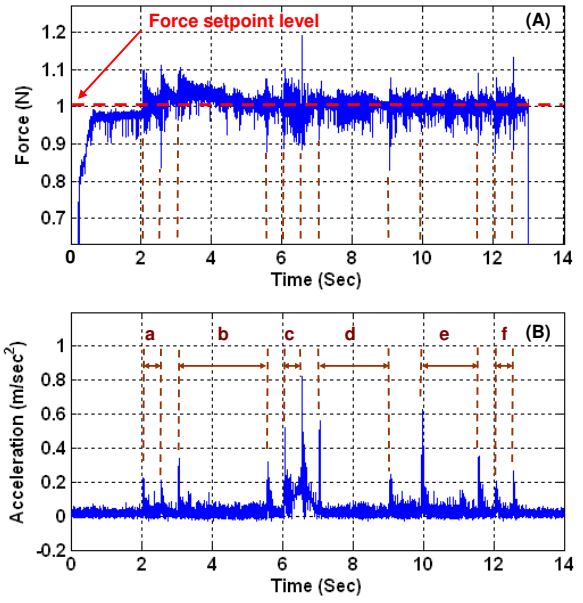

Fig. 18. Experimental results of force control during manipulation tasks (A) Grasp force measured by a finger with FBG sensors (B) Acceleration plotted along with magnitude of combined (X, Y, and Z) acceleration of the robot. Periods a, b, e, and f are for translation motions. Periods c and d are for rotation motions. Every task motion is followed by a waiting period before starting next motions.

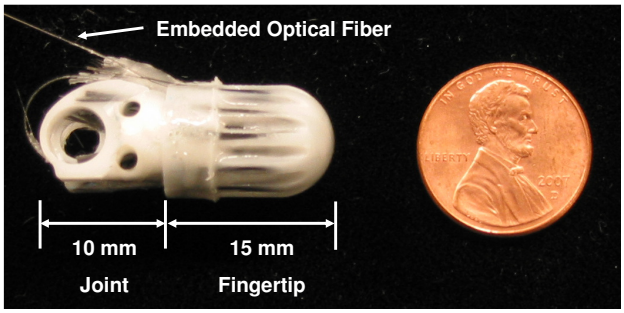

Fig. 19. Miniaturized polyurethane finger prototype fabricated as a hollow shell composed of several curved ribs that are connected at the base by a circular ring and meet at the apex. One optical fiber with four FBG sensors is embedded in the ribs. The structure is reinforced with embedded carbon fibers.

tight bending radii (approximately 7.5 mm). In addition to the optical fibers, carbon fiber was embedded for structural reinforcement and creep reduction.

Figure 20 shows the results of force calibration tests. Applying force up to approximately 5 N to the fingertip yielded sensitivities of 71 pm/N, 54 pm/N, and 7.2 pm/N in X, Y, and Z axes, respectively. Considering the wavelength resolution of the optical interrogator, better than 0.5 pm, the minimum detectable force changes are less than 0.01 N in X and Y axes and 0.07 N in Z axis assuming no temperature changes. The practical resolutions of force measurement are 0.05 N in X and Y axes and 0.16 N in Z axis considering deviations from linearity. Although the current prototype does not contain a temperature compensation sensor, future designs will address temperature compensation as well as increased axial (Z-axis) sensitivity.

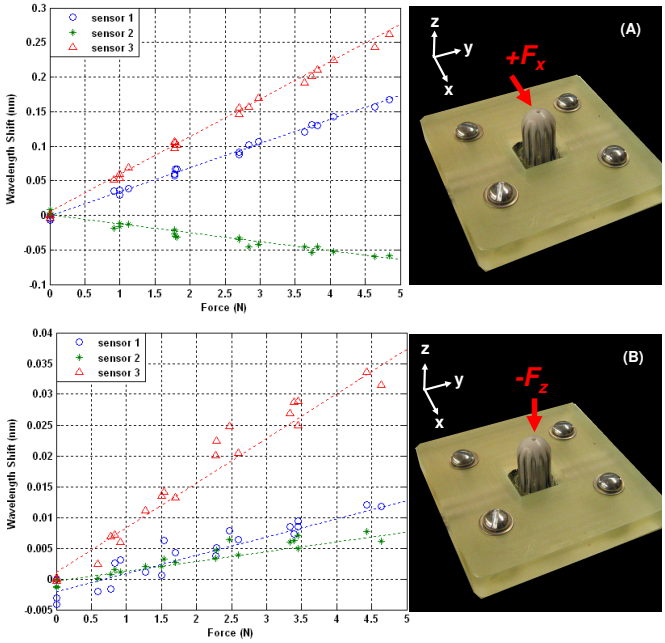

Fig. 20. Calibration results. (A) X axis force response (Y is similar). (B) Z axis force response.

VIII. Optical Interrogation System

The overall interrogator architecture follows that in [39] except that the photonic processor in the present case is based on an arrayed waveguide grating (AWG) technology [40], [48], [59] customized for this application [6]. The approach is based on a parallel photonic processing architecture which has the near-term potential to combine high channel counts ($>$ 100 sensors on a single fiber), high resolution (sub-$\mu\varepsilon$), and high speed ($>$ 5 kHz) with miniaturized footprint. These features will become valuable as we seek to augment the sensor number and response speed of our robot system. The ultimate goal is to have the interrogator integrated into the robotic structure.

As previously discussed, the application of strain on each FBG produces a shift in the selected wavelength, which the interrogator measures. Interrogators can be tunable (examining each FBG sequentially) or parallel in nature. The latter approach, which forms the basis of the our system, has advantages in terms of speed, particularly with many sensors.

The interrogator combines (a) optical signal processing (broadband light source, optical circulator, passive photonic parallel processing chip and photo-detector array) with (b) post-detection electronics, and (c) control and monitoring subsystems as shown in Figure 21. Operation is as follows:

- The broadband source sends light through the optical circulator to an array of FBGs, each of which reflects a different Bragg wavelength.
- The reflected light is returned through the optical circulator to the photonic processor.
- The parallel photonic processor demultiplexes the light into multiple wavelength channels and provides the basis for a ratiometric approach to measuring each of the returned strain-dependent wavelengths.
- The returned wavelengths are converted to arrayed electrical signals by the multi-channel photo detector array.
- Electronics and software provide the final conversion of the arrayed signals to wavelengths and the strains.

The parallel photonic processor used in our interrogator is based on Planar Lightwave Circuit (PLC) and phased-array technology. Optical (and potentially optoelectronic) integration technology allows for fabrication of the photonic processor as

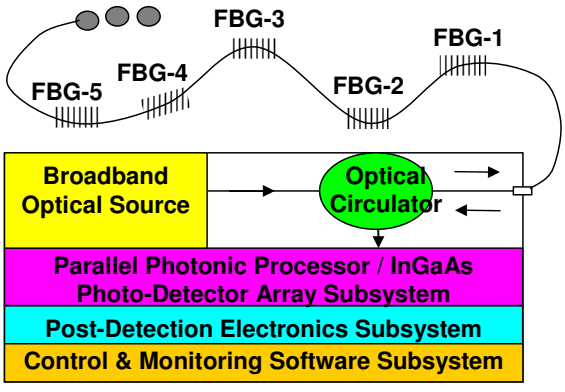

Fig. 21. Functional diagram of FBG interrogator based on a photonic parallel spectral processor which simultaneously processes signals reflected from all FBGs.

a single mass-producible multi-functional chip. This approach is central to achieving the cost and size reductions that will bring FBG sensing solutions into widespread usage.

IX. Conclusions and Future Work

This article has described the development of exoskeletal force sensing robot fingers using embedded FBG optical sensors. A rapid prototyping process, Shape Deposition Manufacturing, was modified to support the fabrication of hollow, plastic mesh structures with embedded components. The sensors were embedded near the base for high sensitivity to imposed loads. The resulting structure is light and rugged. In initial experiments, the sensorized structure demonstrated minimum detectable force changes of less than 0.02 N and practical force measurement resolutions of less than 0.15 N, and a dominant frequency at 167 Hz. With more precise location of the sensors, higher sensitivities should be possible in the future. We also note that any frequency limit is provided by the mechanical finger system, not the interrogator which can measure dynamic strains to 5 kHz.

A copper mesh in the structure reduces viscoelastic creep and provides thermal shielding. A single FBG temperature compensation sensor at the center of the hollow finger helps to reduce the overall sensitivity to thermal variations. However, the central sensor is sufficiently distant from the exterior sensors that changes in temperature produce noticeable transient signals. This effect can be reduced in the future by using a larger number of sensors and locating thermal compensation sensors near the exterior of the structure, where they undergo the same transient thermal strains as the other sensors.

Experiments were also conducted to investigate the finger prototype's ability to localize contact forces. Although the ability to localize forces with just four exterior sensors is limited, the results show that the mesh does respond globally to point contacts in a predictable way. With a larger number of sensors, more accurate contact localization will be possible. Increasing the number of sensors is relatively straightforward as multiple FBGs can be located along each fiber with multiplexing.

A robot hand with the finger prototypes was operated in a hybrid control scheme. The finger sensors are capable of resolving small forces and are immune to electromagnetic disturbances so that the system can be mounted on a large industrial robot, or in other applications where large magnetic fields are present, without concern for shielding and grounding. In addition, as multiple FBG sensors can be placed along a single fiber and multiplexed optically, it suffices to route a single fiber down the robot arm. The potential for miniaturizing the technology is demonstrated with a second prototype having dimensions comparable to a human fingertip. Future versions of this prototype will incorporate additional sensors for thermal compensation and a modified design for greater sensitivity to axial loads.

In parallel, we have been developing versions of the interrogator [33], [39] to support larger numbers of sensors with high resolution and long-term stability. Some design considerations are discussed in the Appendix. As the FBG technology evolves, we foresee the potential in robotics for bend sensors based on multi-core fibers, as well as the use of polymer FBGs [14] in flexible robotic skins. Another possibility is to use multi-parameter dual Bragg gratings in a polarization-maintaining fiber for multi-axial strain measurements [36].

Appendix

For the range of broadband light sources that we use, the available source bandwidth is between 40 nm and 100 nm. Thus, if we make use of the entire available source spectrum and allocate 2 nm per sensor, we can support 20-50 sensors on a single fiber. This number can be increased by using multiple fibers. More precisely, the number of sensors, $N_{sensors}$, that can be supported on a single fiber is related to the source bandwidth, $\delta\lambda_{source}$, divided by the bandwidth required for each sensor, $\delta\lambda_{sensor}$. Further, $\delta\lambda_{sensor}$ is given by the maximum strain-dependent wavelength shift, $\delta\lambda_{strain-max}$, and the sensor wavelength separation, to avoid crosstalk (i.e., to keep it below a "tolerable" level, $\delta\lambda_{cross-talk}$). Thus,

$$N_{sensors} = \frac{\delta\lambda_{source} - |\delta\lambda_{TU}|}{\delta\lambda_{\mathrm{strain-max}} + \delta\lambda_{cross-talk} + \delta\lambda_{TN}}.$$

If the photonic processor is maintained at a constant temperature, while the FBGs see a varying temperature, while the FBGs see a varying temperature, then the effective source bandwidth if reduced by the term $\delta\lambda_{TU}$ which is the maximum FBG wavelength shift due to temperature change, typically 10 pm/°C. Thus, for a 100°C tempearature change, this term results in a 10% reduction in $N_{sensors}$ for $\delta\lambda_{source}$ = 100 nm. If all sensors see the same temperature variation, then they shift uniformly with temperature. On the other hand, if sensors that are adjacent in wavelength see different temperatures, then the spacing needs to be increased by $\delta\lambda_{TN}$, the non-uniform or differential temperature-dependent wavelength shift. For 10°C variation between sensors, $N_{sensors}$ decreases by one third.

The wavelength separation to avoid crosstalk, $\delta\lambda_{\mathrm{cross-talk}}$, (to the extent that wavelength change in one grating does not produce a "measurable" change in the wavelength computed for the adjacent grating) will depend on the FBG spectrum and the parallel spectral processor channel spectra (spacing, bandwidths and shape) as well as the desired measurement precision, but is typically on the order of one to two times the channel separation. Table II summarizes the possible sensor numbers for different source bandwidths and maximum strain-dependent wavelength shifts assuming 0.8 nm for the parallel processor wavelength separation and $\delta\lambda_{cross-talk}$.

TABLE II
Typical sensor numbers that can be supported for a range of spectral characteristics and strain requirements

$\delta\lambda_{source}$	$\delta\lambda_{\mathrm{strain-max}}$	$N_{sensors}$		
		$\delta\lambda_{TU} = 0°\mathrm{C}$ $\delta\lambda_{TN} = 0°\mathrm{C}$	100°C 0°C	100°C 10°C
100 nm	1.2 nm (→1000 $\mu\varepsilon$)	50	45	30
	9.2 nm (→7700 $\mu\varepsilon$)	10	9	8
40 nm	1.2 nm (→1000 $\mu\varepsilon$)	20	15	10
	9.2 nm (→7700 $\mu\varepsilon$)	4	3	2

ACKNOWLEDGEMENT

The authors thank NASA for financial support through SBIR contract NNJ06JA36C and NASA technical monitor Toby Martin for his support and feedback. Special thanks are also due to the late Dr. H. Seraji of NASA's Jet Propulsion Laboratory for his contributions to the project.

REFERENCES

[1] M. Amano, Y. Okabe, N. Takeda, and T. Ozaki. Structural health monitoring of an advanced grid structure with embedded fiber Bragg grating sensors. *Structural Health Monitoring*, 6(4):309–324, 2007.

[2] L. Ascari, P. Corradi, L. Beccai, and C. Laschi. A miniaturized and flexible optoelectronic sensing system for a tactile skin. *International Journal of Micromechanics and Microengineering*, 17:2288–2298, 2007.

[3] F. G. Barth. Spider mechanoreceptors. *Current Opinion in Neurobiology 2004*, 14:415–422, 2004.

[4] F. G. Barth and J. Stagl. The slit sense organs of arachnids. *Zoomorphologie*, 86:1–23, 1976.

[5] A. Bicchi and G. Canepa. Optimal design of multivariate sensors. *Measurement Science and Technology*, 5:319–332, 1994.

[6] R. J. Black and B. Moslehi. Fiber Bragg grating interrogators for structural health monitoring. *Proceedings of the Society for the Advancement of Materials and Process Engineering (SAMPE'08)*, 2008.

[7] R. J. Black, D. Zare, L. Oblea, Y-L. Park, B. Moslehi, and C. Neslen. On the gage factor for optical fiber grating strain gages. *Proceedings of the Society for the Advancement of Materials and Process Engineering (SAMPE'08)*, 53, 2008.

[8] R. Blickhan and F. G. Barth. Strains in the exoskeleton of spiders. *Journals of Comparative Physiology A*, 157:115–147, 1985.

[9] W. Bluethmann, R. Ambrose, M. Diftler, S. Askew, E. Huber, M. Goza, F. Rehnmark, C. Lovchik, and D. Magruder. Robonaut: A Robot designed to work with humans in space. *Autonomous Robots*, 14:179–197, 2003.

[10] L. Carvalho, J. C. C. Silva, R. N. Nogueira, J. L. Pinto, H. J. Kalinowski, and J. A. Simöes. Application of Bragg grating sensors in dental biomechanics. *The Journal of Strain Analysis for Engineering Design*, 41(6):411–416, 2006.

[11] L. A. Danisch, K. Englehart, and A. Trivett. Spatially continuous six degree of freedom position and orientation sensor. *Sensor Review*, 19(2):106–112, 1999.

[12] L. A. Danisch and E. M. Reimer. World patent of canadian space agency. pages PCT, Wo. 99, No.04234, 1999.

[13] C. R. Dennison, P. M. Wild, M. F. Dvorak, D. R. Wilson, and P. A. Cripton. Validation of a novel minimally invasive intervertebral disc pressure sensor utilizing in-fiber Bragg gratings in a porcine model: An ex vivo study. *Spine*, 33(17):E589–E594, 2008.

[14] H. Dobb, D. J. Webb, K. Kalli, A. Argyros, M. C. J. Large, and M. A. van Eijkelenborg. Continuous wave ultraviolet light-induced fibre Bragg gratings in few-and single-moded microstructured polymer optical fibres. *Optics Letters*, 30(24):3296–3298, 2006.

[15] A. Dollar, C. R. Wagner, and R. D. Howe. Embedded sensors for biomimetic robotics via shape deposition manufacturing. *Proceedings of the first IEEE/RAS-EMBS International Conference on Biomedical Robotics and Biomechatronics (BioRob2006)*, 2006.

[16] W. Ecke, I. Latka, R. Willsch, Reutlinger A., and R. Graue. Fiber optic sensor network for spacecraft health monitoring. *Measurement Science and Technology*, 12(7):974–980, 2001.

[17] A. F. Fernandez, F. Berghmans, B. Brichard1, P. Mégret, M. Decréton, M. Blondel, and A. Delchambre. Multi-component force sensor based on multiplexed fibre Bragg grating strain sensors. *Measurement Science and Technology*, 12:810–813, 2001.

[18] R. F. Foelix. Biology of spiders, Second edition. *Oxford University Press US*, 1996.

[19] E. J. Friebele, C. G. Askins, A. B. Bosse, A. D. Kersey, H. J. Patrick, W. R. Pogue, M. A. Putnam, W. R. Simon, F. A. Tasker, W. S. Vincent, and S. T. Vohra. Optical fiber sensors for spacecraft applications. *Smart Materials and Structures*, 8:813–838, 1999.

[20] W. Griffin, W. M. Provancher, and M. R. Cutkosky. Feedback strategies for telemanipulation with shared control of object handling forces. *Presence: Teleoperations and Virtual Environments, MIT Press*, 14(6):720–731, 2005.

[21] T. C. Hales. The honeycomb conjecture. *1999, Available: http://arxiv.org/abs/math.MG/9906042*, 1999.

[22] K. O. Hill and G. Meltz. Fiber Bragg grating technology fundamentals and overview. *Journal of Lightwave Technology*, 15(8):1263–1276, 1997.

[23] N. Hogan. Impedence control: An approach to manipulation, parts i-iii. *ASME Journal of Dynamic Systems, Measurement, and Control*, 107(1):1–24, 1985.

[24] J. Hong and X. Tan. Calibrating a VPL dataglove for teleoperating the utah/mit hand. *Proceedings of the 1989 IEEE International Conference on Robotics and Automation*, 3:1752–1757, 1989.

[25] J. Jung, H. Nam, B. Lee, J. O. Byun, and N. S. Kim. Fiber Bragg grating temperature sensor with controllable sensitivity. *Applied Optics*, 38(13):2752–2754, 1999.

[26] K. Kamiyama, H. Kajimoto, M. Inami, N. Kawakami, and S. Tachi. Development of a vision-based tactile sensor. *IEEJ Transactions on Sensors and Micromachines*, 123(1):16–22, 2003.

[27] H. Kazernooni, T. B. Sheridan, and P. K. Houpt. Robust compliant motion for manipulators, parts i-ii. *IEEE Transactions of Robotics and Automation*, RA-2(2):83–105, 1986.

[28] A. D. Kersey, M. A. Davis, H. J. Patrick, M. LeBlanc, K. P. Koo, C. G. Askins, M. A. Putnam, and E. J. Friebele. Fiber grating sensors. *Journal of Lightwave Technology*, 15(8):1442–1463, 1997.

[29] J. M. Ko and Y. Q. Ni. Technology developments in structural health monitoring of large-scale bridges. *Engineering Structures*, 27(12):1715–1725, 2005.

[30] H-N. Li, D-S. Li, and G-B. Song. Recent applications of fiber optic sensors to health monitoring in civil engineering. *Engineering Structures*, 26(11):1647–1657, 2004.

[31] X. C. Li and F. Prinz. Metal embedded fiber Bragg grating sensors in layered manufacturing. *Journal of Manufacturing Science and Engineering*, 125:577–585, 2003.

[32] G. Liu and Z. Li. A unified geometric approach to modeling and control of constrained mechanical systems. *IEEE Transactions on Robotics and Automation*, 18(4):574–587, 2002.

[33] C. Lopatin, E. Mendez, B. Moslehi, R. J. Black, K. Chau, and L. Oblea. Progress in miniaturization of a multichannel optical fiber Bragg grating sensor interrogator. *Proceedings of SPIE Third European Workshop on Optical Fibre Sensors*, 6619:66193x1–66193x4, 2007.

[34] H. Maekawa, K. Tanie, and K. Komoriya. Tactile feedback for multifingered dynamic grasping. *IEEE Control Systems Magazine*, 17(1):63–71, 1997.

[35] S. Magne, S. Rougeault, M. Vilela, and P. Ferdinand. State-of-strain evaluation with fiber Bragg grating rosettes: application to discrimination between strain and temperature effects in fiber sensors. *Applied Optics*, 36(36):9437–9447, 1997.

[36] T. Mawatari and D. Nelson. A multi-parameter Bragg grating fiber optic sensor and triaxial strain measurement. *Smart Materials and Structures*, pages 1–19, 2008.

[37] D. T. Moran, K. M. Chapman, and R. S. Ellis. The fine structure of cockroach campaniform sensilla. *The Journal of Cell Biology*, 48:155–173, 1971.

[38] W. W. Morey, G. Meltz, and J. M. Weiss. Recent advances in fiber-grating sensors for utility industry applications. *Proceedings of SPIE, Self-Calibrated Intelligent Optical Sensors and Systems*, 2594:90–98, 1996.

[39] B. Moslehi, R. J. Black, K. Toyama, and H. J. Shaw. Multiplexible fiber-optic strain sensor system with temperature compensation capability. *Divisions 1-3*, U.S. Patents 6,895,132, (issued May 17, 2005), 6,788,835, issued Sept 7, 2004, 6,597,822 (issued July 22, 2003).

[40] D. C. C. Norman, D. J. Webb, and R. D. Pechstedt. Extended range interrogation of wavelength division multiplexed fiber Bragg grating sensors using arrayed waveguide grating. *Electronics Letters*, 39:1714–1715, 2003.

[41] S. Pal, J. Mandal, T. Sun, K. T. V. Grattan, M. Fokine, F. Carlsson, P. Y. Fonjallaz, S. A. Wade, and S. F. Collins. Characteristics of potential fibre Bragg grating sensor-based devices at elevated temperatures. *Measurement Science and Technology*, (14):1131–1136, 2003.

[42] Y-L. Park, K. Chau, R. J. Black, and M. R. Cutkosky. Force sensing robot fingers using embedded fiber Bragg grating sensors and shape deposition manufacturing. *Proceedings of the 2007 IEEE International Conference on Robotics and Automation*, pages 1510–1516, 2007.

[43] Y-L. Park, S. Elayaperumal, B. L. Daniel, E. Kaye, K. B. Pauly, R. J. Black, and M. R. Cutkosky. MRI-compatible haptics: Feasibility of using optical fiber Bragg grating strain-sensors to detect deflection of needles in an MRI environment. *International Society for Magnetic Resonance in Medicine (ISMRM) 2008, 16th Scientific Meeting and Exhibition*, 2008.

[44] Y-L. Park, S. C. Ryu, R. J. Black, B. Moslehi, and M. R. Cutkosky. Fingertip force control with embedded fiber Bragg grating sensors.

Proceedings of the 2008 IEEE International Conference on Robotics and Automation, pages 3431–3436, 2008.

[45] I. Peterson. The honeycomb conjecture. *Science News*, 156(4):60, 1999.

[46] M. Raibert and J. Craig. Hybrid position/force control of manipulators. *ASME Journal of Dynamic Systems, Measurement, and Control*, 102(2):126–133, 1981.

[47] Y. J. Rao. In-fibre Bragg grating sensors. *Measurement Science and Technology*, 8(355-375), 1997.

[48] Y. Sano and T. Yoshino. Fast opticalwavelength interrogator employing arrayed waveguide grating for distributed fiber Bragg grating sensors. *Journal of Lightwave Technology*, 21(1):132–139, 2003.

[49] H. Seraji. A new class of nonlinear PID controllers with robotic applications. *Journal of Robotic Systems*, 15(3):161–181, 1998.

[50] H. Seraji, D. Lim, and R. Steele. Experiments in contact control. *Journal of Robotic Systems*, 13(2):53–73, 1996.

[51] H. Seraji and R. Steele. Nonlinear contact control for space station dexterous arms. *Proceedings of the 1998 IEEE International Conference on Robotics and Automation*, 1:899–906, 1998.

[52] E-A. Seyfarth, W. Eckweiler, and K. Hammer. Proprioceptors and sensory nerves in the legs of a spider, *Cupiennius salei* (Arachnida, Araneida). *Zoomorphologie*, 105:190–196, 1985.

[53] D. S. Smith. The fine structure of haltere sensilla in the blowfly Calliphora erythrocephala (Meig.) with scanning electron microscopic observations on the haltere surface. *Tissue and Cell*, 1:443–484, 1969.

[54] J. S. Son, M. R. Cutkosky, and R. D. Howe. Comparison of contact sensor localization abilities during manipulation. *Proceedings of 1995 IEEE/RSJ International Conference on Intelligent Robots and Systems*, 2:96–103, 1995.

[55] R. Suresh, S. C. Tjin, and S. Bhalla. Multi-component force measurement using embedded fiber Bragg grating. *Optics and Laser Technology*, doi:10.1016/j.optlastec.2008.08.004, 2008.

[56] N. Takahashi, A. Hirose, and S. Takahashi. Underwater acoustic sensor with fiber Bragg grating. *Optical Review*, 4(6):691–694, 1997.

[57] R. M. Voyles, G. Fedder, and P. K. Khosla. Design of a modular tactile sensor and actuatator based on an electrorheological gel. *Proceedings of the 1996 IEEE International Conference on Robotics and Automation*, 1:13–17, 1996.

[58] L. E. Weiss, R. Merz, F. B. Prinz, G. Neplotnik, P. Padmanabhan, L. Schultz, and K. Ramaswami. Shape deposition manufacturing of heterogenous structures. *Journal of Manufacturing Systems*, 16(4):239–248, 1997.

[59] G. Z. Xiao, P. Zhao, F. G. Sun, Z. G. Lu, Z. Zhang, and C. P. Grover. Interrogating fiber bragg grating sensors by thermally scanning an arrayed waveguide grating based demultiplexer. *Optics Letters*, 29:2222–2224, 2004.

[60] M. G. Xu, J-L. Archambault, L. Reekie, and J. P. Dakin. Discrimination between strain and temperature effects using dual-wavelength fibre grating sensors. *Electronics Letters*, 30(13):1085–1087, 1994.

[61] M.G. Xu, L. Dong, L. Reekie, J.A. Tucknott, and J.L. Cruz. Temperature-independent strain sensor using a chirped Bragg gratingin a tapered optical fibre. *Electronics Letters*, 31(10):823–825, 1995.

[62] G. Zeng and A. Hemami. An overview of robot force control. *Robotica*, 15:473–482, 1997.

[63] L. Zhang, J. Qian, Y. Zhang, and L. Shen. On SDM/WDM FBG sensor net for shape detection of endoscope. *Proceedings of the 2005 IEEE International Conference on Robotics and Automation*, 4:1986–1991, 2005.

[64] W. Zhang, E. Li, J. Xi, J. Chicharo, and X. Dong. Novel temperature-independent FBG-type force sensor. *Measurement Science and Technology*, 16:1600–1604, 2005.

Yong-Lae Park (S' 07) received the B.S. degree in industrial engineering from Korea University, Seoul, Korea, in 2000, and the M.S. degree in mechanical engineering from Stanford University, Stanford, CA, in 2005, where he is currently pursuing the Ph.D. degree in mechanical engineering.

His current research interests include fiber optic force and tactile sensing of robot manipulators for space and medical applications, design of haptic master-slave systems for minimally invasive surgery robots, and 3-D smart robot structure development.

Seok Chang Ryu received the B.S. degree in mechanical engineering from POSTECH, Pohang, Korea, in 2002, and the M.S. degree in mechanical engineering from Stanford University, Stanford, CA, in 2007, where he is currently pursuing the Ph.D. degree in mechanical engineering.

His professional experience includes development of trajectory planners for SCARA and wafer-transfer robots at Robostar Co., LTD, Seoul, Korea. His research interest is medical application of robots.

Richard J. Black (M' 82) received the B.Sc. (Hons.) degree in physics from the University of Canterbury, New Zealand, and the Ph.D. degree in fiber optics from the Research School of Physical Sciences at the Australian National University.

He is a founding member of and Chief Scientist at Intelligent Fiber Optic Systems Corporation (IFOS) and the founder of OptoSapiens Design. His present work focuses on optical fiber sensing systems with application to structural health monitoring, robotics and medical devices. He is a member of AAAI, ACM, ASM, IEEE, OSA, SPIE and SAMPE.

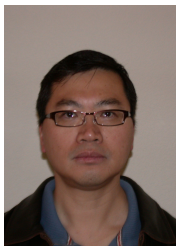

Kelvin K. Chau received his B.S. degree in Engineering Physics/Optics from University of California, San Diego, CA, in 1985, and the M.S. degree in Electrical Engineering from San Jose State University, San Jose, CA, in 1990.

His professional experience includes complex optoelectronic system integration and product development. He is currently with Glimmerglass Networks, leading the development of high-port-count 3-D optical MEMS switches for commercial applications.

Behzad Moslehi received the B.S. degree in electrical engineering from Arya-Mehr University of Technology, Tehran, Iran, in 1978, and the M.S. degree in electrical engineering, in 1980, the M.S. degree in applied physics and the Ph.D. degree in electrical engineering, in 1984, all from Stanford University, Stanford, CA.

His research includes photonic signal processing, sensing, communications and networking for applications in avionics, safety, life sciences, and energy. He is the founder and CEO/CTO of Intelligent Fiber Optic Systems Corporation (IFOS). He is a member of IEEE, OSA, SPIE, SAMPE, SPE, AWEA, and Sigma Xi.

Mark R. Cutkosky (M' 92) received the Ph.D. in mechanical engineering from Carnegie Mellon University, Pittsburgh, PA, in 1985. He is a Professor in Mechanical Engineering at Stanford University.

His research interests include robotic manipulation and tactile sensing and the design and fabrication of biologically inspired robots. His awards include a Fulbright Faculty Chair, Charles M. Pigott Professorship and NSF Presidential Young Investigator award. He is a member of IEEE, ASME and Sigma Xi.